Excitation of the shear horizontal mode in a monolayer by inelastic helium atom scattering

Bruch, L. W.; Hansen, Flemming Yssing

Published in:
Journal of Chemical Physics

Link to article, DOI:
10.1063/1.1869416

Publication date:
2005

Document Version
Publisher's PDF, also known as Version of record

Excitation of the shear horizontal mode in a monolayer by inelastic helium atom scattering

L. W. Bruch
Department of Physics, University of Wisconsin-Madison, Madison, Wisconsin 53706

F. Y. Hansen
Department of Chemistry, Technical University of Denmark, IK-207-DTU, DK-2800 Lyngby, Denmark

(Received 9 November 2004; accepted 19 January 2005; published online 24 March 2005)

Inelastic scattering of a low-energy atomic helium beam (HAS) by a physisorbed monolayer is treated in the one-phonon approximation using a time-dependent wave packet formulation. The calculations show that modes with shear horizontal polarization can be excited near high symmetry azimuths of the monolayer, in agreement with recent experiments. The parameters of the calculations are chosen to match the conditions of HAS experiments for triangular incommensurate monolayer solids of xenon, krypton, and argon adsorbed on the (111) face of platinum, and the results show many of the systematic experimental trends for relative excitation probability of the shear horizontal and longitudinal acoustic phonon branches. The inelastic scattering at beam energies near 8 meV is exceedingly sensitive to small misalignment between the scattering plane and the high symmetry directions of the monolayer solid. The diffraction and inelastic processes arise from a strong coupling of the incident atom to the target and the calculated results show large departures from expectations based on analogies to inelastic thermal neutron scattering.
 [DOI: 10.1063/1.1869416]

I. INTRODUCTION

The excitation spectrum of a solid can provide a detailed test of the understanding of the underlying interactions. Thus, experiments that measure the excitation energies of normal modes (i.e., phonon energies) of a solid give fundamental information on how a macroscopic system is built up from its atomic and molecular constituents. The goal of this paper is to determine whether the one-phonon inelastic scattering approximation, using realistic interactions, is adequate to reproduce the main features and trends in a comprehensive body of experimental helium atom scattering data which show the excitation of all three branches [shear horizontal (SH), longitudinal acoustic (LA), and perpendicular (S)] of the monolayer vibrations.

There are significant advantages to using thermal energy particle beams to probe the excitation spectrum of simple solids, because the energy transfers are large fractions of the incident particle energy and hence can be determined accurately. This has been exploited systematically with inelastic neutron scattering,[1,2] where leading order perturbation theory provides an adequate formulation of the process. The situation is far less satisfactory for thermal energy helium atom scattering (HAS), and the assignment of observed dispersive branches of physisorbed monolayer solids has been in dispute.[3,4] The central point of the discussion is that basic polarization selection rules appear to preclude the excitation of modes with SH polarization in the monolayer plane or, at least, strongly diminish their intensities relative to those for modes with LA polarization.

Some HAS experiments on xenon monolayers were interpreted[3,5] as showing that the interaction energy between two monolayer atoms is greatly changed from that for an isolated xenon pair. Nevertheless, if the polarization selection rule is ignored, observed spectra for monolayers of xenon, krypton, or argon can be understood in terms of unperturbed adatom-adatom forces.[6] Experiments on the Rayleigh wave and other surface modes of thick films of solid xenon were analyzed[7] in terms of unperturbed xenon-xenon forces and the observation there of SH excitations was attributed to a polarization mixing arising from coupling of the first xenon layer to the underlying layers. The observation of SH excitations in other systems was attributed to symmetry-breaking effects arising from defects.

However, in experiments[6] with xenon and krypton adsorbed on the (111) face of platinum, Pt(111), the monolayer solids displayed an orientational epitaxy[8] that usually is seen only for highly ideal monolayer conditions. Further, for helium beam energies below 10 meV, the SH branch was excited with much greater probability than the LA branch. These facts suggest that an explanation must involve more than small symmetry-breaking terms.

We have discovered that the inelastic scattering probabilities at incident beam energies 8.2–8.5 meV are exceedingly sensitive to small misalignment of the scattering plane relative to the high symmetry axes ΓM and ΓK of the monolayer solid. Alignments along the orientational epitaxy angles of 2.6° and 5.3° for Xe/Pt(111) and Kr/Pt(111), respectively, (i.e., along symmetry axes of the bulk Pt crystal) lead to large excitation probabilities for SH modes at small wave number. Even for nominally aligned solids of Kr/Pt(111) and Ar/Pt(111), the observed spread of alignments includes angles α large enough to enable easily exciting the SH mode. The remarkable result of our strong coupling scattering

theory is that the probability of exciting SH modes can be greater than that for LA modes already at such small angles α that analogies to the neutron scattering theory would suggest a very small relative probability for SH relative to LA.

Dense phases of inert gases have been important test cases of statistical mechanical theories of bulk liquids and solids because the pair potentials are known[9] and many-body interactions are rather small for the three-dimensional solids. Similar treatments of adsorption-induced interactions for the monolayer solids reproduced a large body of data.[10] The interaction of a helium atom with monolayer inert gas solids also is given primarily by sums of pair potentials. This has been demonstrated by analysis of the selective adsorption resonance levels of helium interacting with a monolayer of xenon on the basal plane of graphite[11] and on Ag(111).[12]

Thus the interactions for the coupled helium–adsorbed monolayer system are well-determined inputs to the scattering calculations. We use them without further adjustments, except to include the small effect of the McLachlan adsorption-induced interactions on the harmonic lattice dynamics of the monolayer solids.[10,13] Because we assert that the known scattering theory and known interactions suffice to reproduce the strong low-energy excitation probability of the SH modes, we make few approximations in implementing the theory, to demonstrate that the effect is intrinsic and does not require invoking uncharacterized defects.

The organization of this paper is as follows: Sec. II contains the formulation of the scattering theory and Sec. III contains a description of the computational methods and the components of the model. Salient features of the experimental data are reviewed in Sec. IV. Results of the calculations are presented in Sec. V and discussed in Sec. VI. Final remarks are given in Sec. VII.

II. THEORY

A. One-phonon approximation

The Hamiltonian operator for inelastic scattering of an atom a by the monolayer solid is

$$H = K_{\mathrm{kin}} + H_{\mathrm{ph}} + V_c, \tag{1}$$

where K_{kin} is the kinetic energy operator of the incident (helium) atom of mass m_a and H_{ph} is the Hamiltonian of the monolayer solid treated in the harmonic approximation. H_{ph} is expressed in phonon operators as

$$H_{\mathrm{ph}} = \sum_{\vec{Q},\lambda} \hbar\omega(\vec{Q},\lambda) a^{+}(\vec{Q},\lambda) a(\vec{Q},\lambda), \tag{2}$$

with a sum over wave vectors $\vec{Q}$ in the first Brillouin zone and branches λ. The ground state of H_{ph} is denoted Φ_0. The sum of the atom-monolayer and atom-substrate potential energies is denoted $V_c = V_s + V_d$. It consists of a static part V_s with all monolayer atoms at their equilibrium positions and a dynamic part V_d arising from the vibrational displacements of the atoms. Dynamic coupling[14] of the monolayer and substrate is neglected.

The solution to the time-dependent Schrödinger equation

$$\imath\hbar\, \partial\Psi/\partial t = H\Psi \tag{3}$$

is taken to have the form $\Psi = \Psi_0 + \Psi_1$ where the elastically scattered (diffractive) component Ψ_0 satisfies

$$\imath\hbar\, \partial\Psi_0/\partial t = H_0\Psi_0, \tag{4}$$

$$H_0 = K_{\mathrm{kin}} + H_{\mathrm{ph}} + V_s. \tag{5}$$

The inelastic scattering component in the one-phonon approximation[15,16] is the solution of

$$\imath\hbar\, \partial\Psi_1/\partial t = H_0\Psi_1 + V_1\Psi_0, \tag{6}$$

where a term $V_d\Psi_1$ is neglected and V_1 is an expansion of V_d to first order in monolayer atom displacements, i.e., multiphonon processes are omitted.

For helium-adatom potentials $\phi(|\vec{R}|)$, the Steele decomposition of the potential energy with the static monolayer is, with reciprocal lattice vectors $\vec{g}$ and area per adatom A_c,[10]

$$V_s(\vec{r},z) = V_0(z) + \sum_{\vec{g}} V(\vec{g},z)\exp(\imath\vec{g}\cdot\vec{r}), \tag{7}$$

$$V(\vec{g},z) = (1/A_c)\int d^2r\, \exp(-\imath\vec{g}\cdot\vec{r})\,\phi(\sqrt{r^2+z^2}). \tag{8}$$

The components of the helium position vector parallel and perpendicular to the monolayer plane are denoted $\vec{r}$ and z, respectively. Additionally, V_0 includes the helium-substrate van der Waals energy $-C_3/z^3$.

The corresponding expression for V_1 is obtained by writing the monolayer atom displacements $\vec{\rho}_j$ in terms of normal mode coordinates (angular frequencies ω and polarization unit vectors $\hat{e}$) and the phonon creation and annihilation operators (and N is the number of atoms of mass m in the monolayer):

$$\vec{\rho}_j = \sum_{\vec{Q},\lambda} \sqrt{\hbar/2mN\omega(\vec{Q},\lambda)}\,\hat{e}(\vec{Q},\lambda) \times\exp(\imath\vec{Q}\cdot\vec{R}_j)[a(\vec{Q},\lambda) + a^{+}(-\vec{Q},\lambda)]. \tag{9}$$

The operator is then

$$V_1 = \sum_{\vec{Q},\lambda,\vec{g}} C_\lambda(\vec{g}+\vec{Q},z)\exp[\imath(\vec{g}+\vec{Q})\cdot\vec{r}]a(\vec{Q},\lambda) + C^{*}_\lambda(\vec{g}+\vec{Q},z)\exp[-\imath(\vec{g}+\vec{Q})\cdot\vec{r}]a^{+}(\vec{Q},\lambda), \tag{10}$$

where the coefficients are

$$C_\lambda(\vec{g}+\vec{Q},z) = -\sqrt{\hbar/2mN\omega(\vec{Q},\lambda)}\,\hat{e}(\vec{Q},\lambda) \cdot\left[\imath(\vec{g}+\vec{Q})V(\vec{g}+\vec{Q},z) + \hat{z}\frac{dV(\vec{g}+\vec{Q})}{dz}\right]. \tag{11}$$

The expansion of Ψ_0 in terms of diffraction channels for elastic scattering from a target in its ground state Φ_0 is, for initial parallel wave vector $\vec{K}$,

$$\Psi_0 \equiv \tilde{\Psi}_0 \Phi_0 = \sum_{\vec{g}} \psi_{\vec{g}}(z,t) \exp[\imath(\vec{g}+\vec{K})\cdot\vec{r}]\Phi_0. \tag{12}$$

The Schrödinger equation for the coupled channel functions is

$$\imath\hbar \frac{\partial \psi_{\vec{g}}}{\partial t} = \frac{\hbar^2}{2m}\left\{(\vec{g}+\vec{K})^2 - \frac{\partial^2}{\partial z^2}\right\}\psi_{\vec{g}} + \sum_{\vec{g}_2} V(\vec{g}-\vec{g}_2,z)\psi_{\vec{g}_2}. \tag{13}$$

The wave function Ψ_1 for one-phonon creation is

$$\Psi_1 = \sum_{\vec{Q},\lambda} \psi_{\vec{Q},\lambda} a^+(\vec{Q},\lambda)\Phi_0, \tag{14}$$

and the Schrödinger equation for the channel functions is

$$\imath\hbar \frac{\partial \psi_{\vec{Q},\lambda}}{\partial t} = [K_{\mathrm{kin}} + V_s + \hbar\omega(\vec{Q},\lambda)]\psi_{\vec{Q},\lambda} + \sum_{\vec{g}} C^*_{\lambda}(\vec{g}+\vec{Q},z)\exp[-\imath(\vec{g}+\vec{Q})\cdot\vec{r}]\tilde{\Psi}_0. \tag{15}$$

The dependence of each channel function on $\vec{r}$ again is expanded using the two-dimensional (2D) reciprocal lattice vectors:

$$\psi_{\vec{Q},\lambda} = \sum_{\vec{g}} \exp[\imath(\vec{K}-\vec{Q}+\vec{g})\cdot\vec{r}]S_{\vec{Q},\lambda}(\vec{g},z,t), \tag{16}$$

and the equations that actually are integrated are

$$\imath\hbar \frac{\partial S_{\vec{Q},\lambda}(\vec{g},z,t)}{\partial t} = \left[\frac{\hbar^2}{2m}\left\{(\vec{K}-\vec{Q}+\vec{g})^2 - \frac{\partial^2}{\partial z^2}\right\} + \hbar\omega(\vec{Q},\lambda)\right]S_{\vec{Q},\lambda}(\vec{g},z,t) + \sum_{\vec{g}_2} V(\vec{g}-\vec{g}_2,z)S_{\vec{Q},\lambda}(\vec{g}_2,z,t) + \sum_{\vec{g}_2} C_{\lambda}(\vec{g}-\vec{g}_2-\vec{Q},z)\psi_{\vec{g}_2}(z,t). \tag{17}$$

In the following, the monolayer is assumed to be a triangular lattice with one atom per unit cell, nearest neighbor spacing L and area $A_c=\sqrt{3}L^2/2$, and three branches λ, denoted SH, LA, and S. The SH and LA branches are polarized primarily in the monolayer plane and the S branch perpendicular z to the plane.

The scattering event is followed as a function of time, starting from an initial wave function with a Gaussian wave packet for motion in the z direction:[17,18]

$$\Psi_i(\vec{r},z) = (2A/\pi)^{1/4}\exp(\imath[k_{iz}(z-z_0)+\vec{K}_i\cdot\vec{r}]) \times \exp(-A[z-z_0]^2). \tag{18}$$

The total initial energy of this normalized function, $E_i = \hbar^2(k_{iz}^2+\vec{K}_i^2+A)/2m$, includes the small spread about the central wave number k_{iz}. In the calculations, A is taken to be small enough that the incident wave is rather monochromatic, and the initial packet center z_0 is placed so that most of the starting configuration is outside the range of interaction with the monolayer and substrate.

The coupled linear differential equations for the wave packet propagation are solved using a fast Fourier transform for the kinetic energy[18] and a simple stepping procedure for the time integration:

$$\psi(t+dt) = \psi(t-dt) + \left.\frac{\partial\psi}{\partial t}\right|_t (2dt). \tag{19}$$

The time integration is accurate through second order in dt and is very stable. The inelastic scattering calculation has parallel solutions for the elastic scattering Ψ_0 and the three polarization branches in Ψ_1.

B. Scattering rate

The solutions to Eq. (17) are used to form channel norms

$$N_{\vec{Q},\lambda}(\vec{g},t) = \int |S_{\vec{Q},\lambda}(\vec{g},z,t)|^2 dz \tag{20}$$

and the corresponding averages and variances of z. The limiting value of $N_{\vec{Q},\lambda}$ at large time (t_f=20 ps for $E_i \approx 8$ meV, 14 ps for E_i=16.6 meV) is taken to be proportional to the probability of the inelastic scattering event.[19]

Final scattering rates incorporate some additional factors. First, they are defined in terms of the fluxes, so that the scattering probability is multiplied by a factor k_f/k_{iz}, where k_f and k_{iz} are the final wave number and perpendicular component of the initial wave vector.[20] Second, the coupling V_1, Eq. (10), has a sum over $\vec{Q}$ and there is an energy conserving δ function when this is converted to an integration:

$$\sum_{\vec{Q}} \rightarrow (NA_c)/(2\pi)^2 \int d\vec{Q}\,\delta[E_f + \hbar\omega(\vec{Q},\lambda) - E_i]. \tag{21}$$

A special feature of scan-curve constraints in the experiments, Sec. IV B, is that E_f depends on $\vec{Q}$ and there is a factor

$$1/|\partial(E_f+\hbar\omega)/\partial Q|$$

which, when singular, leads to kinematical focussing.[20] This effect does not occur for the conditions treated here. There also is a factor for the out-of-scattering-plane resolution. Of these factors, only k_f is included in comparing our calculations to experiments[6] for which the intensity data were not corrected for the effect of k_{iz}. The others should be incorporated in the future for more complete modeling of the experiments.

C. Thermal effects

The theory in Secs. II A and II B is for a monolayer at zero temperature. At finite temperature,[2,21] the intensities are modified by Debye–Waller factors. The Debye–Waller factor on inelastic intensities for a harmonic monolayer solid is, with perpendicular and parallel momentum transfers Δk_z and $\Delta\vec{K}$, respectively,[2]

$$F_{DW} = \exp\{-(\Delta k_z)^2\langle\rho_z^2\rangle - \Delta\vec{K}\cdot\langle\vec{\rho}\vec{\rho}\rangle\cdot\Delta\vec{K}\}. \quad (22)$$

The $\langle\cdots\rangle$ denotes a thermal average.[22] F_{DW} is dominated by the Δk_z term for the conditions of the low-energy HAS experiments.[6]

An important contribution to the systematic dependence of the experimental inelastic scattering intensities on $|\vec{Q}|$ arises from another effect of the thermally excited phonons in the target monolayer. The phonon creation matrix element has a factor[21] $\sqrt{1+n[\omega(\vec{Q},\lambda)]}$ arising from the action of $a^+(\vec{Q},\lambda)$ on a state of occupation number $n[\omega(\vec{Q},\lambda)]$. Then the thermally averaged intensities are multiplied by a factor

$$f_{\vec{Q},\lambda}(T) \equiv 1 + \overline{n}[\omega(\vec{Q},\lambda)] = 1/\{1-\exp[-\hbar\omega(\vec{Q},\lambda)/k_BT]\}. \quad (23)$$

Consequently, the intensities for the SH and LA branches at small $|\vec{Q}|$ are enhanced relative to those calculated with the zero temperature theory. In Sec. V, the calculated products $I_c(\vec{Q},\lambda)=k_fN_{\vec{Q},\lambda}f_{\vec{Q},\lambda}(T)F_{DW}$, with $\vec{g}=0$ and $t=t_f$, are compared to experimental scattering intensities.

III. IMPLEMENTATION

A. Methods and diagnostics

In the implementation, the infinite sums over coupled channels are truncated, a grid is established for the z coordinate, and a time step dt is chosen. Sensitivity tests are performed for the xenon layer at incident energies of 8.2 and 16.6 meV to see that the accuracy of the calculation is preserved.

The spatial grid extends from $z=1.5$ Å (relative to the monolayer plane) to 124 Å in steps $dz=0.06$ Å. The large range for z is needed so that a spatially wide, rather monochromatic, initial wave packet [$1/A=72$ Å^2 in Eq. (18)] can be started at $z_0\approx 24$ Å, outside the interaction region, and propagated for $\approx$20 ps to make the elastic scattering event go to completion. Figure 1 shows examples of the laterally averaged probability density for elastic scattering, $\Sigma_{\vec{g}}|\psi_{\vec{g}}(z)|^2$, constructed from $|\Psi_0|^2$ at three propagation times.

The time step is linked to the spatial grid. For too large a time step, the propagation becomes unstable, as evidenced by a failure to conserve the total normalization of Ψ_0. The step chosen, $dt=0.04$ fs, is small compared to that frequently used in other propagation schemes,[17] but the simplicity of our algorithm meant that in practice the total running (CPU) time was only moderately longer than with more sophisticated propagators. The basic propagation scheme applies also to the inelastic scattering calculation and to arbitrary azimuths for the scattering plane.

The sum over coupled channels in the elastic scattering includes all open channels and closed channels with lateral kinetic energy up to about three times the incident kinetic energy. At 8 meV, there are 45–55 channels (Ar–Xe) and at 16.6 meV (Xe) there are $\approx$95 channels.[23]

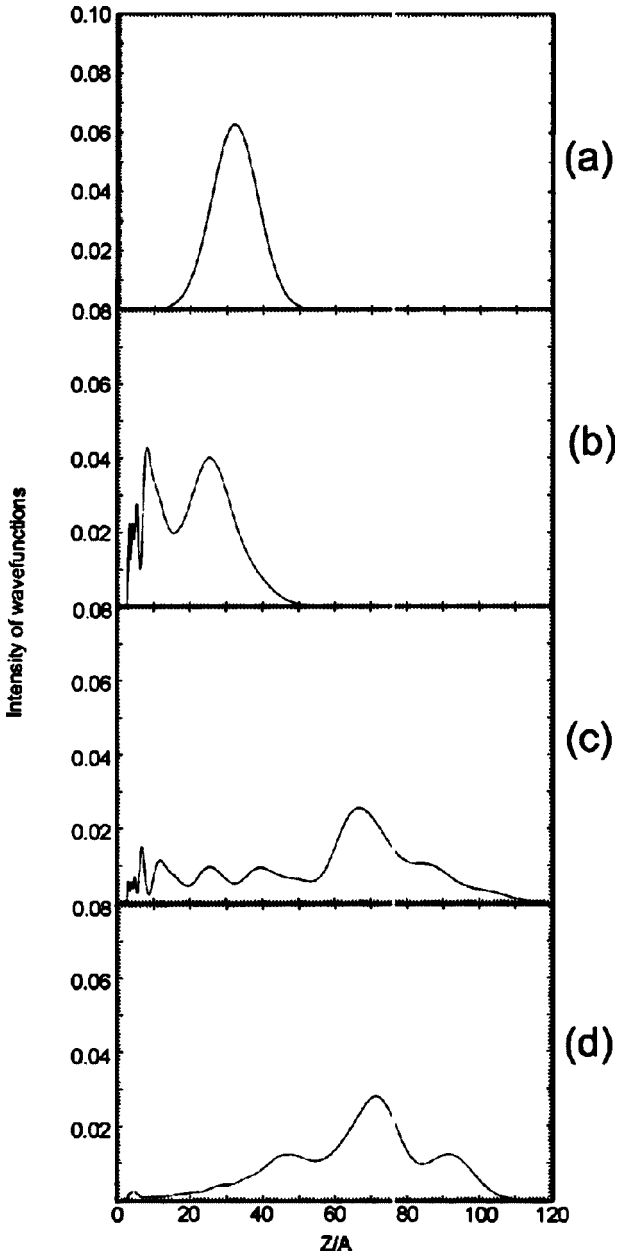

FIG. 1. Laterally averaged probability density for elastic scattering by a xenon monolayer at $E_i=8.2$ meV at specified angles of incidence ϑ_i. $\Sigma_{\vec{g}}|\psi_{\vec{g}}|^2$ is shown as a function of perpendicular distance z (in Å) for three propagation times. (a) Initial state, Eq. (18) with $1/A=72$ Å^2, at $t=0$. (b) $\vartheta_i=45.2°$, $\alpha=0.5°$ relative to the ΓM axis, at $t=10$ ps. 80.3% of the norm is in open channels. (c) As in (b), at $t=20$ ps. There still is only 92.6% of the norm in open channels. (d) $\vartheta_i=44.2°$, $\alpha=2.6°$ relative to the ΓK axis, at $t=20$ ps. 99.4% of the norm is in open channels.

Diagnostics for the diffracted wave function Ψ_0 include: total norm, total energy, expectation value of z and its variance, and the norms and expectation values and variance of z for each of the $\vec{g}$ channels.

Further diagnostics for the one-phonon wave function Ψ_1 include: norm and expectation value and variance of z for each polarization in each $(\vec{g}+\vec{Q})$ channel. At 100 fs intervals, there is an analysis identifying the major contributors to the driving term $V_1\Psi_0$ feeding the $\vec{g}=0$ channel (i.e., the parallel momentum transfer is $\vec{Q}$).

TABLE I. Parameters of the scattering experiments at incident energy E_i and target temperature T and the interaction models. The monolayers have nearest neighbor spacings L_{nn}, S-mode energies $\omega_\perp$, and are aligned as specified. ϵ and $R_{\min}$ are the depth and separation of the helium-adatom pair potential. $V_0(\min)$ and $z_{\min}$ are the corresponding parameters for $V_0(z)$ defined at Eq. (7).

Property	Xe/Pt(111)	Kr/Pt(111)	Ar/Pt(111)
E_i(meV)	8.2	8.4	8.5
T(K)	50±5	50±5	23±5
L_{nn}(Å)	4.33	4.09	3.79
L_{ov}(Å)[a]	2.2	1.8	1.7
$\omega_\perp$(meV)	3.5	3.85	4.85
Alignments[b]	2.6°R30	5.0°R30, 2°R0	2°R0
ϵ(meV)[c]	2.49	2.63	2.55
$R_{\min}$(Å)	3.96	3.69	3.50
$V_0(\min)$(meV)[d]	−7.76	−8.45	−8.90
$z_{\min}$(Å)	3.52	3.26	3.09

[a]Monolayer height above the electrodynamic boundary of the substrate, used in calculating the He–Pt van der Waals energy, $-C_3/(z+L_{ov})^3$, and the McLachlan terms.
[b]Alignment of a primitive space lattice vector of the monolayer relative to the axis of the substrate (R0) or to the axis for a $\sqrt{3}$ commensurate monolayer (R30). The values for R0 are within the range of an observed continuous range of alignments.
[c]Aziz and Tang-Toennies models, Refs. 11 and 27.
[d]This includes the contribution from the He–Pt van der Waals energy.

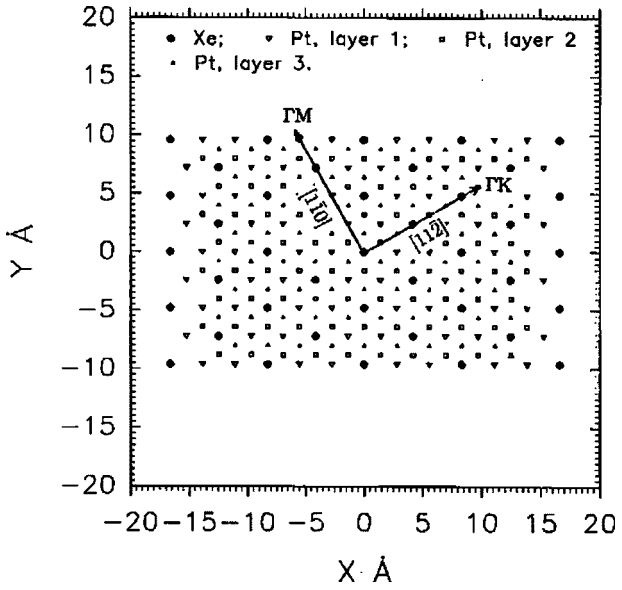

FIG. 2. Schematic diagram for orientation of a commensurate xenon monolayer lattice on Pt(111). The ΓM and ΓK axes of the adlayer are shown. In the notation of this paper, the lattice is aligned with $\alpha=0°$ relative to the Pt[1$\bar{1}$0] axis, so that ΓM coincides with Pt[1$\bar{1}$0] and ΓK with Pt[11$\bar{2}$] in this figure. Atomic positions in the first three layers of the Pt(111) surface are marked.

B. Interactions and lattice dynamics

The normal modes of the monolayer solids are evaluated using atom-atom potentials constructed by Aziz and co-workers[24–26] and supplemented by the McLachlan substrate-mediated dispersion energy.[10,13] The monolayers are assumed to be regular planar triangular lattices, incommensurate with the substrate. Vibrations perpendicular to the monolayer plane decouple from those in the plane and are nearly dispersionless. The lattice constants, overlayer spacings, and S-mode frequencies $\omega_\perp$ are listed in Table I. The pair potentials between the helium atom and monolayer atoms are the HFD-B2 for He–Xe Ref. 11 and the TT03 potentials[27] for He–Kr and He–Ar. The strength of the He–Pt(111) van der Waals energy is $C_3=0.0632$ a.u., using the Rauber approximation.[10]

For the analysis of conditions where intense SH excitations are found, the bound states of the 1D Hamiltonian $p_z^2/2m_a+V_0(z)$ are calculated for the three monolayers. These are good approximations to the selective adsorption resonance levels.[28]

IV. SALIENT FEATURES OF THE EXPERIMENTS

A. Trends in the data

We first review the data[6] for the incommensurate monolayers Xe/Pt(111), Kr/Pt(111), and Ar/Pt(111). Two scattering planes were used, containing the [11$\bar{2}$] and [1$\bar{1}$0] Pt azimuths. Figure 2 is a schematic diagram showing the identification of axes for the special case of a commensurate monolayer Xe/Pt(111).

The excitation process depends more on the orientation of the scattering plane relative to the monolayer than relative to the substrate. The strongest signals for SH modes are when the scattering plane is near the ΓM axis of the monolayer rather than when it is near the ΓK axis. This is found for Xe/Pt(111), where the ΓM axis is at 2.6° to the Pt[1$\bar{1}$0] axis. It holds for Kr/Pt(111) both when the ΓM axis is at 5.3° to Pt[1$\bar{1}$0] and when it is nearly aligned with Pt[11$\bar{2}$]. It also holds for Ar/Pt(111) where the ΓM axis is nearly aligned with Pt[11$\bar{2}$]. The azimuthal full width at half-maximum for diffracted intensity is[6] about 5.8° for Ar/Pt(111), and it is even broader[29] for the Kr/Pt(111) case along Pt[11$\bar{2}$].

For wave vectors $\vec{Q}$ near the ΓM axis the excitation probability of the SH mode is largest for $|\vec{Q}|<0.2$ Å^{-1}, where the differences relative to the ΓK axis are most pronounced, and decreases at larger $|\vec{Q}|$. At the smallest $|\vec{Q}|$, the SH probability seems to be strongest for the Ar monolayer.

The SH branch is quite readily excited for incident helium energies of 8.2–8.5 meV, but it is nearly undetectable at beam energies of 16.6 meV and higher.

The LA branch is not very well resolved at $E_i\approx 8$ meV, but it is definitely observed for $E_i\approx 17$ meV. However, the LA branches of these monolayer solids lie so close to the Rayleigh wave branch of Pt(111) that no quantitative measures of the intensity variation were given. Qualitatively, the LA branch intensity at $E_i\approx 8$ meV definitely was less than that of the SH branch.

The SH branch is excited for parallel momentum transfers in the first Brillouin zone, in contrast to the neutron scattering experiments and other HAS experiments.[30]

B. Scan-curve constraints

The HAS instruments typically[31] have a fixed angle Θ_{SD} between the incident and final helium atom momenta. Hence,

TABLE II. Calculated channel norms Eq. (20) for inelastic scattering by monolayers at conditions specified in Table I. The quantity $NN_{\vec{Q},\lambda}(\vec{g},t_f)$ is given for $\vec{g}=0$ and $t_f=20$ or 14 ps, according to the initial beam energy E_i. N is the number of adatoms, see Eq. (11). The azimuthal orientation α of the scattering plane relative to monolayer axes ΓM and ΓK is given for each case; the polar angle of incidence ϑ_i is chosen to satisfy scan-curve constraints as described in Sec. V A.

Case	E_i(meV)	Q(Å^{-1})	SH(ΓM)	SH(ΓK)	LA(ΓM)	LA(ΓK)	S(ΓM)	S(ΓK)
Xe 2.6°	8.2[a]	0.125	0.0135	0.0085	0.0082	0.0020	0.0535	
		0.25	0.0074	0.0022	0.0117	0.0016	0.0422	0.102
		0.4	0.0042					
	16.6[b]	0.125	0.0064	0.0084	0.0021	0.0006	0.0610	0.0481
		0.25	0.0032	0.0014	0.0018	0.0005	0.0342	0.0444
		0.5			0.0024			
Kr 5.0°	8.4[a]	0.125	0.0298	0.0221	0.0050	0.0180	0.147	
		0.25	0.0402	0.0092	0.0101	0.0036	0.116	
		0.4	0.0094		0.0128		0.131	
Kr 2.0°	8.4[a]	0.125	0.0688	0.0197	0.0062	0.0029	0.149	
		0.25	0.0520	0.0037	0.0184	0.0064	0.0879	
		0.4	0.0445		0.0079		0.129	
Ar 2.0°	8.5[a]	0.125	0.162	0.0257	0.0400	0.0285	0.264	
		0.25	0.137	0.0552	0.0122	0.0171	0.280	
		0.4	0.0185		0.0353		0.331	

[a] $t_f=20$ ps.
[b] $t_f=14$ ps.

at given $\vec{Q}$ and E_i, the angle of incidence ϑ_i of the initial wave vector $\vec{k}_i$ is different for the scatterings that give the SH, LA, and S modes. In the experiments[6] for Pt(111), the angle is $\Theta_{SD}=95.8°$.

The experimental results are presented in terms of the increment in parallel wave vector of the helium atom, $\Delta\vec{K}=\vec{K}_f-\vec{K}_i$, and this is opposite to the wave vector of the phonons. That is, with momentum conservation to within a reciprocal lattice vector, the experimental data give $\Delta\vec{K}=-(\vec{Q}+\vec{g})$. The SH modes are better resolved for "positive" ΔK, $\vec{Q}$ opposite to $\vec{K}_i$, and the intensity variations are best determined for this geometry.[32] In the scattering calculations for the triangular monolayer lattices, where $\omega(-\vec{Q},\lambda)=\omega(\vec{Q},\lambda)$, this distinction enters in the determination of the $\vec{K}_i$ for a scattering leading to excitation of a given $|\vec{Q}|$.

V. RESULTS OF THE CALCULATIONS

A. Excitation of the SH branch at low energies, $E_i \approx 8$ meV

All results here are for scan-curve conditions in which the phonon wave vector $\vec{Q}$ is antiparallel to $\vec{K}_i$ and $\vec{g}=0$. The most extensive calculations are for incident energies near 8 meV and scattering planes aligned relative to monolayer symmetry axes at $\alpha=2.6°$ for xenon, $\alpha=5.0°$ and 2.0° for krypton, and $\alpha=2.0°$ for argon. The first two of these four values correspond to experimental alignments and the latter two are within the observed spread of α in nominally aligned cases.[6,29] The calculations for $|\vec{Q}|=0.125$ and 0.25 Å^{-1} are with scattering planes at angle α relative to both the ΓM and ΓK axes of the monolayer solids. For $|\vec{Q}|=0.4$ Å^{-1}, the calculations are only for the case near ΓM. A summary of the calculated channel norms $N_{\vec{Q},\lambda}$ is presented in Table II.

In Fig. 3, the calculated $I_c(\vec{Q},\lambda)=k_f N_{\vec{Q},\lambda}(\vec{g}=0,t_f)f_{\vec{Q},\lambda}(T)F_{DW}$, $t_f=20$ ps, are compared to experimental data for the inelastic scattering intensities. Each series of calculated values is scaled so that the SH (ΓM) intensity at $|\vec{Q}|=0.125$ Å^{-1} lies on a linear interpolation in the experimental data. Different scaling factors are used for Xe, Kr, and Ar. For Xe ($\alpha=2.6°$) and Ar ($\alpha=2.0°$), calculated SH intensities near ΓM and ΓK and LA intensities near ΓM are shown. For Kr these three intensities are shown for $\alpha=5.0°$ and the SH intensity near ΓM is shown also for $\alpha=2.0°$ (with the same scaling as for 5.0°) to illustrate the strength for a misalignment within the experimental range for an "accidental" krypton monolayer[6] at R0°.

For all pairs that we compared (same E_i and $\vec{Q}$), the intensity of the SH mode is more intense near the ΓM axis than at the same angle to the ΓK axis. This agrees with the experiments.[6]

With one exception (Kr 5.0°, $|\vec{Q}|=0.25$ Å^{-1}), the calculated zero temperature SH intensity at angle $\alpha(\geqslant 2.0°)$ to the ΓM axis decreases monotonically from $|\vec{Q}|=0.125$ Å^{-1} to $|\vec{Q}|=0.4$ Å^{-1}. When the finite temperature correction of Eq. (23) is included, all cases have monotonically decreasing SH intensity on this interval. As shown in Fig. 3, the calculations have an overall trend similar to the experiments for the drop from the peak in SH intensity at small $|\vec{Q}|$. The decrease is less steep than in the experimental data, which also show some more structure at 0.25–0.5 Å^{-1}. The intensity ratio $I_c(0.125\ \text{Å}^{-1},\text{SH})/I_c(0.4\ \text{Å}^{-1},\text{SH})(\vec{g}=0,t_f=20\text{ps})$ is 9 for Xe 2.6° and for Kr 5.0°, 4 for Kr 2.0°, and 21 for Ar 2.0°.

Finally, the calculated intensity of the SH branch

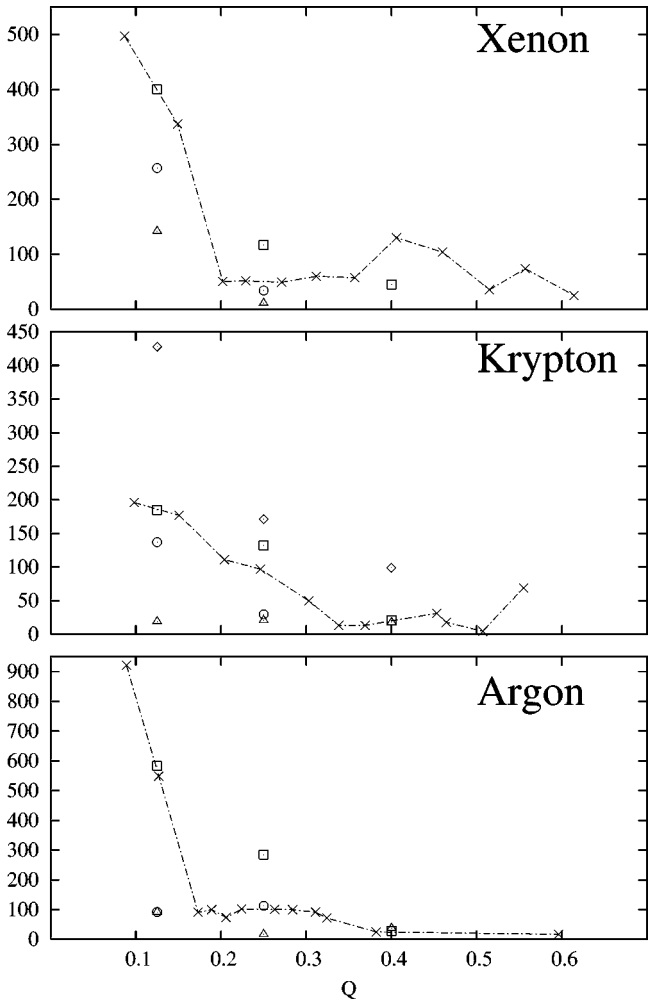

FIG. 3. Comparison of calculated intensities $I_c(\vec{Q},\lambda)=k_f N_{\vec{Q},\lambda}(\vec{g}=0,t_f)f_{\vec{Q},\lambda}(T)F_{DW}$ at $t_f=20$ ps to experimental data (Refs. 6,29) for inelastic helium atom scattering at $E_i\approx 8$ meV as a function of 2D wave vector $\vec{Q}$ in Å^{-1}. Calculated values are shown for SH near ΓM (squares) and ΓK (○) and LA near ΓM (△) at specified misalignment angles α and are scaled to match the experimental SH intensity near ΓM (data points *X* linked by broken line) at $|\vec{Q}|=0.125$ Å^{-1}. (a) Xenon with $\alpha=2.6°$ for both calculation and experiment; (b) krypton with $\alpha=5.3°$ for experiment and $\alpha=5.0°$ and $\alpha=2.0°$ [only SH(ΓM), ◇] for calculation; (c) argon with $\alpha=0°$ (experiment) and $\alpha=2.0°$ (calculation). The $\alpha=2.0°$ cases of the calculation are within the range of alignments observed for the corresponding nominally aligned layers.

$I_c(\vec{Q},\mathrm{SH})$ is larger than that for the LA branch $I_c(\vec{Q},\mathrm{LA})$ at $|\vec{Q}|=0.25$ and 0.125 Å^{-1}, especially for the azimuths near (but $\alpha\geqslant 2°$) the ΓM axis. The variation of $I_c(\vec{Q},\mathrm{LA})$ with $|\vec{Q}|$ differs in several cases, but there is a trend for it to become comparable to or larger than $I_c(\vec{Q},\mathrm{SH})$ when $|\vec{Q}|\approx 0.4$ Å^{-1}. Remarkably, $I_c(\vec{Q},\mathrm{SH})$ is comparable to the calculated S-branch intensity $I_c(\vec{Q},\mathrm{S})$ for $|\vec{Q}|=0.25$ and 0.125 Å^{-1} under scan-curve conditions.

B. Inelastic scattering at intermediate energy, $E_i\approx 17$ meV

Our only calculations at intermediate energy are for Xe 2.6° at 16.6 meV. The calculated SH branch intensities are within 50% of the values for 8.2 meV, when comparisons are made at the same $\vec{Q}$, in contrast to the experimental data, which have very much smaller intensities. The LA branch intensities are much smaller for $|\vec{Q}|\leqslant 0.25$ Å^{-1}. A calculation for $|\vec{Q}|=0.5$ Å^{-1} near the ΓM axis did show an appreciable intensity for the LA branch. The S-branch $\omega_\perp$ intensity was 50%–100% larger at 16.6 meV, comparing at the same $\vec{Q}$, but this seems to be a less pronounced increase than in the experiments.

C. Perfectly aligned scattering plane

It was expected,[5] on the basis of quite general symmetry arguments, that there should be no excitation probability for the SH modes at wave vectors in the first Brillouin zone when the scattering plane is oriented along the high symmetry monolayer axes ΓM and ΓK, i.e., for $\alpha=0$. This is also the result in our calculations.

However, inspection of the components of the inhomogeneous term in Eq. (17) for the $\vec{g}=0$ channel function of the xenon layer at $E_i=8.2$ meV shows there are large and precisely canceling $\vec{g}_2\neq 0$ contributions at $\alpha=0$. A small misalignment is sufficient to lead to a substantial net contribution. For $|\vec{Q}|=0.125$ Å^{-1} and near the ΓM axis, the final SH intensity at $\alpha=0.5°$ is already half of its value for $\alpha=2.6°$.

D. Further analysis

With only one exception (Xe, $Q=0.125$ Å^{-1}, 16.6 meV), the calculated SH intensity is larger for scans near ΓM than ΓK when results for the same $|\vec{Q}|$ are compared at the same final run time t_f (20 ps for ≈8 meV and 14 ps for 16.6 meV). The enhancement near ΓM relative to ΓK is correlated to geometry of the reciprocal lattice. There is a substantial persisting norm for channels closed by energy margins 1 meV or less and these occur more frequently for the ΓM alignments.

We examined the relative importance of the mixing term $V(\vec{g}-\vec{g}_2)$ and the source term C_λ in Eq. (17) on the evolution of the SH inelastic intensity. For xenon at 8.2 meV, the total SH norm (summed over all channels) is near its limit already at 10–14 ps, but the norm in the $\vec{g}=0$ channel still increases to the end of the calculation at 20 ps. There were cases for which this latter increase clearly came by conversion from other channels, but in general it seemed that there was continuing contribution from the part of Ψ_0 that had lingered near the monolayer.

Another point is the role of the van der Waals He–Pt potential C_3 in the interaction model. The minimum of $V_0(z)$ is 20%–35% deeper (Xe–Ar) than for a model with $C_3=0$ and the deepest selective adsorption state (bound state in V_0) is 30%–50% deeper. In calculations comparing the scattering for xenon at 8.2 meV, the total diffracted intensity after 16 ps is smaller by up to 2% with the full model. The most pronounced effect is in the calculated $\tilde{z}$ for scattering plane near ΓM. At $Q=0.125$ Å^{-1} the difference is 6 Å out of 45 Å and is consistent with an increased role of transient trapping near the monolayer in the deeper potential.

The calculated SH excitation probability for the xenon monolayer is greater for the $E_i=8.2$ meV than at 16.6 meV.

However, the excitation probability must decrease as E_i is reduced further to the energy threshold $\hbar\omega(Q,\mathrm{SH})$. We have not done the systematic calculations needed to identify the optimal E_i, which maximizes the excitation probability.

VI. DISCUSSION

The three monolayers treated here, Ar/Pt(111), Kr/Pt(111), and Xe/Pt(111), are very corrugated targets for thermal energy ^{4}He beams. This is shown by the intense peaks both in diffraction experiments and in the calculations, where the specularly reflected beam [$\vec{g}=0$ term of Ψ_0, Eq. (12)] for $E_i \approx 8$ meV has only about 10% of the total intensity.

Another signature of the strong coupling effects in the calculations is that the elastic scattering of the wave packet, especially at $E_i \approx 8$ meV, takes a long time to go to completion. For instance, there are several cases[33] where the fraction of the normalization of Ψ_0 in open channels is still only 0.9–0.95 at 20 ps. Bittner and Light[34] noted a related phenomenon, an increased lifetime for the scattered particle near the surface, in their calculations of ^{4}He scattering by a monolayer of Xe/Ag(111). Cases of incomplete elastic scattering at 20 ps correlate rather well with those where there are large probabilities for excitation of SH modes. Examples of incomplete and nearly complete elastic scattering events are shown in Figs. 1(c) and 1(d), respectively.

The present strong coupling calculations are computationally intensive. The question arises how much of the physics might be recovered with a more approximate theory such as distorted wave Born approximation (DWBA).[35] As presently implemented,[5,7,21] the distorted wave is the solution in the laterally averaged potential V_0, Eq. (7), and the absence of SH excitations in the calculations then follows quite directly from a vanishing scalar product $\vec{Q}\cdot\hat{\epsilon}(\vec{Q},\mathrm{SH})$. If a full close coupling solution[11,12] for the diffracted wave Ψ_0 were made, including the misalignment $\alpha \neq 0$, we anticipate that the DWBA would reproduce qualitatively the main features of our calculations. We tested for the importance of the corrugation term ($\vec{g}_2 \neq 0$) in the driving term C_λ in Eq. (17) for two xenon cases, $Q=0.25$ Å^{-1} at 2.6° from ΓM and $Q=0.125$ Å^{-1} at 0.5° from ΓM. Even for the LA and S excitation probabilities, which are nonzero already in the DWBA calculations,[5] there were major changes in the intensities in the first Brillouin zone, $\vec{g}=0$. With the $\vec{g}_2 \neq 0$ terms removed, the LA intensities were, respectively, a factor of 0.2 and 1.2 times the result of the full calculation and the S intensity was reduced by about 60%. This is another indication of the strong coupling effects.

There is a sensitivity of the inelastic intensities to the angle of incidence ϑ_i. The orientation of $\vec{k}_i$ is different for the scan curve at given $\vec{Q}$ for the three polarizations, and in several cases the ratio of SH to LA intensities varied by 50% as ϑ_i varied. The conditions for strong SH excitation do not appear to correspond to resonances with bound ^{4}He states: the energies of closed channels with long-lived norm mostly deviated from the selective adsorption bound states by more than 0.1 meV. They do correlate with conditions where channels closed by energy margin of less than 1 meV are populated.

VII. CONCLUSIONS

The SH branch can be readily excited in HAS experiments at low incident energies without invoking effects of defects or of second layer gas above the monolayer solid. The effect is not special to xenon layers and is strong for argon and krypton layers too. We have shown that a small misalignment angle α of the scattering plane relative to high symmetry axes of the monolayer has large effects on the excitation of SH modes. The misalignment might arise from orientational epitaxy of the monolayer relative to the substrate, as in the cases treated here, or from a misalignment of the orientation of the substrate itself.[36] Recognizing the significant role of the misalignment should resolve much of the difficulty that arose from applying polarization selection rules to previous DWBA solutions.

There are many directions for systematic extension of the present calculations. They should be extended to lower beam energies, getting closer to energetic thresholds for the inelastic scattering. The $E_i \approx 8$ meV results are in fair agreement with the experiments but the results for the LA and S branches at $E_i \approx 17$ meV suggest there may be additional effects not yet included. Coincidentally, the potentials $V_0(z)$ are very similar for Xe, Kr, and Ar, so it will be of interest to have calculations for a case with much shallower attractive well, such as a monolayer solid of H_2.[36]

The theory of the inelastic scattering has now developed far enough that there will be much more capability for modeling future inelastic atom scattering experiments. We expect to extend the present line of work to include a more thorough treatment at intermediate incident energy, especially for excitation of the S branch, and to better characterize the transient trapping phenomenon.

ACKNOWLEDGMENTS

This work was partially supported by NSF under Grant No. DMR0104300. Extensive discussions with Dr. A. P. Graham about the experimental conditions were most helpful. In the early stages of this project the authors benefited from discussions with the late Professor G. D. Billing. The authors thank Professor L. Tribe for discussions of alternative approaches to calculate the diffractive scattering.

[1] B. N. Brockhouse, Rev. Mod. Phys. **67**, 735 (1995).
[2] W. Marshall and S. W. Lovesey, *Theory of Thermal Neutron Scattering* (Oxford University Press, Oxford, 1971).
[3] A. P. Graham, M. F. Bertino, F. Hofmann, J. P. Toennies, and C. Wöll, J. Chem. Phys. **106**, 6194 (1997); **107**, 4445 (1997).
[4] L. W. Bruch, J. Chem. Phys. **107**, 4443 (1997).
[5] A. Šiber, B. Gumhalter, J. Braun, A. P. Graham, M. Bertino, J. P. Toennies, D. Fuhrmann, and C. Wöll, Phys. Rev. B **59**, 5898 (1999), and references cited therein.
[6] L. W. Bruch, A. P. Graham, and J. P. Toennies, J. Chem. Phys. **112**, 3314 (2000).
[7] A. Šiber, B. Gumhalter, A. P. Graham, and J. P. Toennies, Phys. Rev. B **63**, 115411 (2001).
[8] A. D. Novaco and J. P. McTague, Phys. Rev. Lett. **38**, 1286 (1977).
[9] *Inert Gases: Potentials, Dynamics, and Energy Transfer in Doped Crys-*

tals, edited by M. L. Klein (Springer, Berlin, 1984); *Rare Gas Solids*, edited by M. L. Klein and J. A. Venables (Academic, London, 1976).
[10]L. W. Bruch, M. W. Cole, and E. Zaremba, *Physical Adsorption: Forces and Phenomena* (Oxford University Press, Oxford, 1997).
[11]R. A. Aziz, U. Buck, H. Jónsson, J.-C. Ruiz-Suárez, B. Schmidt, G. Scoles, M. J. Slaman, and J. Xu, J. Chem. Phys. **91**, 6477 (1989); **93**, 4492(E) (1990).
[12]K. D. Gibson, C. Cerjan, J. C. Light, and S. J. Sibener, J. Chem. Phys. **88**, 7911 (1988).
[13]A. D. McLachlan, Mol. Phys. **7**, 381 (1964). The coefficients C_{s1} and C_{s2} are given in Table II of Ref. 6.
[14]B. Hall, D. L. Mills, P. Zeppenfeld, K. Kern, U. Becher, and G. Comsa, Phys. Rev. B **40**, 6326 (1989), and references cited therein.
[15]B. H. Choi and R. T. Poe, J. Chem. Phys. **83**, 1330 (1985).
[16]D. Eichenauer, U. Harten, J. P. Toennies, and V. Celli, J. Chem. Phys. **86**, 3693 (1987).
[17]D. Lemoine, Comput. Phys. Commun. **97**, 331 (1996); R. B. Gerber, R. Kosloff, and M. Berman, Comput. Phys. Rep. **5**, 59 (1986).
[18]N. E. Henriksen, G. D. Billing, and F. Y. Hansen, Chem. Phys. Lett. **199**, 176 (1992).
[19]The distinction between the square of the Fourier amplitude for final wave vector $\vec{k}_f$ and the norm is small for these nearly monochromatic wave packets.
[20]J. P. Toennies, in *Surface Phonons*, Springer Series in Surface Sciences Vol. 21, edited by W. Kress and F. W. de Wette (Springer, Berlin, 1991), p. 111.
[21]B. Gumhalter, Phys. Rep. **351**, 1 (2001).
[22]The calculations are done using the classical approximation for in-plane motions and summing over the discrete wave vectors, $\vec{Q} \neq 0$ and periodic boundary conditions, of a 60° parallelopiped 2000 lattice constants on a side. See Sec. 4.2.3 of Ref. 10 for a review of the effects of thermal fluctuations in mathematical two dimensions.
[23]The number of $\vec{g}$ channels is determined by the condition $(\hbar^2/2m)(\vec{K}_i + \vec{g})^2 \leqslant E_i - E_c$, with parameters $\vec{K}_i$ and E_i defined at Eq. (18). The value of the cutoff energy E_c is increased until elastic scattering intensities have converged and is $E_c = -170$ K($\simeq -14.6$ meV) for $E_i = 8.2-8.5$ meV and $E_c = -250$ K($\simeq -21.5$ meV) for $E_i = 16.6$ meV.
[24]A. K. Dham, W. J. Meath, A. R. Allnatt, R. A. Aziz, and M. J. Slaman, Chem. Phys. **142**, 173 (1990).
[25]R. A. Aziz and M. J. Slaman, Mol. Phys. **58**, 679 (1986).
[26]A. K. Dham, A. R. Allnatt, W. J. Meath, and R. A. Aziz, Mol. Phys. **67**, 1291 (1989).
[27]K. T. Tang and J. P. Toennies, J. Chem. Phys. **118**, 4976 (2003).
[28]M. W. Cole and F. Toigo, Phys. Rev. B **23**, 3914 (1981); S. Chung, N. Holter, and M. W. Cole, *ibid.* **31**, 6660 (1985).
[29]A. P. Graham, private communication.
[30]A. Glebov, W. Silvestri, J. P. Toennies, G. Benedek, and J. G. Skofronick, Phys. Rev. B **54**, 17866 (1996).
[31]A. P. Graham, Surf. Sci. Rep. **49**, 115 (2003).
[32]Kinematic focussing becomes a possibility for "negative" ΔK, Ref. 20.
[33]It is not a simple matter to extend the calculations to long enough times that the total diffracted intensity in open channels is close to unity for all cases. Already, there are several cases where this intensity is larger than 0.99. However there also are cases where it is in the range 0.90–0.95 and extending the time of propagation by 20% did not increase it significantly. Much of the diffracted wave Ψ_0 is nearing the large-z end of the range, already quite large for such work, and there will be a need for be major modifications to the method to cope with the extreme trapping cases.
[34]E. R. Bittner and J. C. Light, J. Chem. Phys. **101**, 2446 (1994).
[35]V. Celli, in *Surface Phonons*, edited by W. Kress and F. W. de Wette (Springer, Berlin, 1991), Chap. 6, G. Santoro and V. Bortolani, in *Inelastic Energy Transfer in Interactions with Surfaces and Adsorbates*, edited by B. Gumhalter, A. C. Levi, and F. Flores (World Scientific, Singapore, 1993), pp. 1–38; J. R. Manson and V. Celli, Surf. Sci. **24**, 495 (1971).
[36]F. Traeger and J. P. Toennies, J. Phys. Chem. B **108**, 14710 (2004), and Ref. 49 therein.